Dynamics of liquid drops coalescing in the inertial regime

James E. Sprittles[*]

Mathematics Institute, University of Warwick, Coventry CV4 7AL, United Kingdom

Yulii D. Shikhmurzaev[†]

School of Mathematics, University of Birmingham, Birmingham B15 2TT, United Kingdom

We examine the dynamics of two coalescing liquid drops in the "inertial regime," where the effects of viscosity are negligible and the propagation of the front of the bridge connecting the drops can be considered as "local." The solution fully computed in the framework of classical fluid mechanics allows this regime to be identified, and the accuracy of the approximating scaling laws proposed to describe the propagation of the bridge to be established. It is shown that the scaling law known for this regime has a very limited region of accuracy, and, as a result, in describing experimental data it has frequently been applied outside its limits of applicability. The origin of the scaling law's shortcoming appears to be the fact that it accounts for the capillary pressure due only to the longitudinal curvature of the free surface as the driving force for the process. To address this deficiency, the scaling law is extended to account for both the longitudinal and azimuthal curvatures at the bridge front, which, fortuitously, still results in an explicit analytic expression for the front's propagation speed. This expression is shown to offer an excellent approximation for both the fully computed solution and for experimental data from a range of flow configurations for a remarkably large proportion of the coalescence process. The derived formula allows one to predict the speed at which drops coalesce for the duration of the inertial regime, which should be useful for the analysis of experimental data.

I. INTRODUCTION

The rapid motion that ensues after two drops of the same liquid come into contact (Fig. 1) is the key element of a wealth of processes, notably in micro- and nanofluidic devices such as "3D printers," where structures are built using microdrops as building blocks. It is clear, therefore, that understanding the physical mechanisms that govern the drops' coalescence, and being able to predict the motion of the drops during this process, is key for the development of these emerging technologies.

Due to recent advances in both experimental and computational techniques, there has been a surge in the number of publications studying the coalescence of liquid drops in an ambient gas (air) [2–7]. The experimental aspects of the problem have been driven by the application of both ultra-high-speed imaging techniques [3] and a novel electrical method [6], which has circumvented fundamental issues with optical measurements. From a computational perspective, specially designed codes have been used to capture all scales in the problem and to resolve a flow that is known to be singular [1,8]. Notably, most of the aforementioned works have focused on the different "regimes" encountered and the "transitions" between them, typically shown on log-log plots, with the main attention given to formulating or using the correct "scalings" in each regime.

It has now been established that the crossover from the "viscous" or "inertially limited viscous" [1] regime to an "inertial regime," in which viscous forces are negligible compared to inertial ones, occurs when the dimensional radius

r_b of the bridge (Fig. 2) connecting the coalescing drops in the early stages of the process satisfies $\bar{r}_b = r_b/R \sim \mathrm{Re}_i^{-1}$ [6,8], where $\mathrm{Re}_i = \sqrt{\rho \sigma R / \mu^2}$ is the Reynolds number in the inertial regime for a drop of radius R, density ρ, surface tension σ, and viscosity μ. This Reynolds number is related to the Ohnesorge number Oh sometimes used in coalescence studies via $\mathrm{Oh} = \mathrm{Re}_i^{-1}$.

Consider now the bridge radius at which water drops will enter the inertial regime. If the drops are millimeter-sized, $R = 1$ mm, as is often the case in experiments, we have $\mathrm{Re}_i = O(10^2)$ so that the drops enter the inertial regime when $r_b/R = O(10^{-2})$. If instead microdrops are considered with, say, $R = 10\ \mu$m, then $\mathrm{Re}_i = O(10)$ and the bridge radius still needs only to reach $r_b/R = O(10^{-1})$ before the inertial regime is entered. In other words, for low-viscosity liquids such as water, the majority of the dynamics of the bridge (defined, crudely, as $r_b/R > 0.1$) of the coalescence event occurs in the inertial regime, even for the drops encountered in microfluidics. This is the regime that will be considered in this paper.

The inertial regime has previously been studied experimentally, using ultra-high-speed cameras [1–5]; analytically, by developing scaling laws [9] and asymptotic theory [10]; and computationally, considering either the local problem [11], where the initial stages of bridge front propagation are studied independently from the overall flow configuration, *or* the global dynamics of the drops [2,12], where the entire geometry is accounted for. It has been shown theoretically [9], computationally [1,8,11], and experimentally [1–5] that, in this regime, the bridge front propagates with a square root in time scaling. In particular, in [9], the driving capillary pressure $\sigma \kappa$ due to the surface tension and based on the longitudinal curvature $\kappa \sim 1/d(t)$ obtained from the undisturbed free-surface shape of the drops, $d(t) \sim r_b^2(t)/R$, is balanced by

---

[*]J.E.Sprittles@warwick.ac.uk
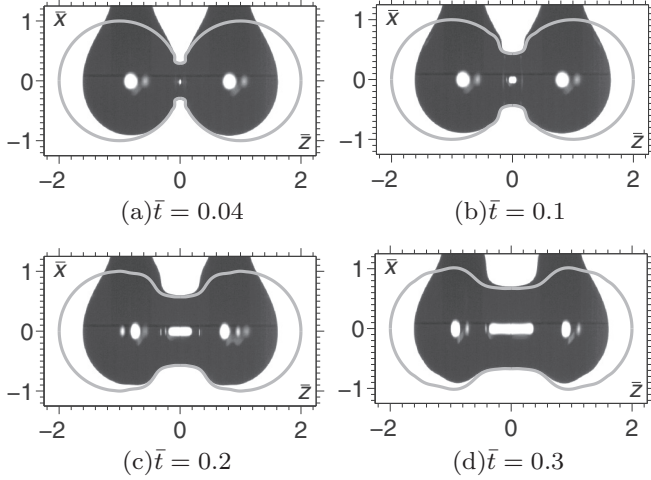
[†]Y.D.Shikhmurzaev@bham.ac.uk

FIG. 1. A typical coalescence event comparing our computations, with free spheres, against experiments in [1] conducted using 1cP pendent drops of silicone oil (one unit of length is $R = 1.1$ mm and one unit of time is $T_i = 8$ ms).

the dynamic pressure, $\rho(dr_b/dt)^2$. As a result, one has $r_b/R = C_i(t/T_i)^{1/2}$, where C_i is a constant of proportionality, so that, once nondimensionalized by our characteristic scales in this regime, that is, R for length and $T_i = \sqrt{\rho R^3/\sigma}$ for time, the scaling law takes the form

$$\bar{r}_b = C_i \bar{t}^{1/2}. \tag{1}$$

Here, and henceforth, all quantities with an overbar are dimensionless.

Our approach here will be to establish the existence of a well-defined inertial regime, to study the accuracy of scaling laws in this regime using the corresponding numerical solution of the full-scale mathematical problem, and to compare their predictions to experimental data from the literature. This will lead us to an improved scaling law for the regime that will be shown to describe experimental data for a much larger period of time than (1) and will allow us to identify previous works where the wrong value of C_i in (1) has been chosen.
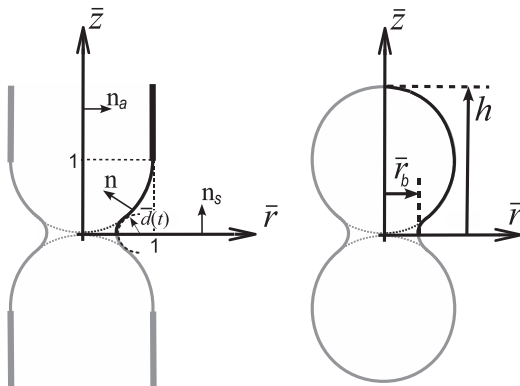

FIG. 2. A definition sketch for the coalescence of two identical "pinned hemispheres" grown from syringes (left) and a sketch of coalescing "free spheres" (right) showing the bridge radius $\bar{r}_b$ and apex height h.

II. PROBLEM FORMULATION

In this work, we will consider both the typical experimental setup in which hemispherical drops are grown from syringes as well as the case of most practical interest, where free spheres coalesce (Fig. 2). Assuming that gravity can be ignored, which is reasonable for mm-sized drops and below [8], the problem becomes symmetric and can be reduced to determining the motion of one drop in the $(\bar{r},\bar{z})$ plane of a cylindrical coordinate system with the symmetry conditions on the $\bar{z} = 0$ plane at which the drops initially touch. The syringe, when considered, is taken to be a semi-infinite cylinder with zero-thickness walls located at $\bar{r} = 1, \bar{z} > 1$. The precise far-field conditions, i.e., those associated with the syringe head, have a negligible effect on the initial stages of coalescence [8].

To nondimensionalize the system of the governing equations for the bulk variables, we use the drop radius R as the characteristic length scale, $U_i = \sqrt{\sigma/(\rho R)}$ as the scale for velocities, $T_i = \sqrt{\rho R^3/\sigma}$ as the time scale, and $\mu U_i/R$ as the scale for pressure. Then, the continuity and momentum balance equations take the form

$$\nabla \cdot \mathbf{u} = 0, \quad \text{Re}_i\left[\frac{\partial \mathbf{u}}{\partial t} + \mathbf{u} \cdot \nabla \mathbf{u}\right] = \nabla \cdot \mathbf{P},$$

$$\mathbf{P} = -p\mathbf{I} + [\nabla \mathbf{u} + (\nabla \mathbf{u})^T], \tag{2}$$

where $\mathbf{P}$, $\mathbf{u}$, and p are the (dimensionless) stress tensor, velocity, and pressure in the fluid, and $\mathbf{I}$ is the metric tensor of the coordinate system. As before, the Reynolds number $\text{Re}_i = \sqrt{\rho \sigma R/\mu^2}$.

The conventional boundary conditions used for free-surface flows are the kinematic condition, stating that the fluid particles forming the free surface stay on the free surface at all time and the balance of tangential and normal forces acting on an element of the free surface from the two bulk phases and from the neighboring surface elements:

$$\frac{\partial f}{\partial \bar{t}} + \mathbf{u} \cdot \nabla f = 0, \tag{3}$$

$$\mathbf{n} \cdot \mathbf{P} \cdot (\mathbf{I} - \mathbf{nn}) = \mathbf{0}, \quad \mathbf{n} \cdot \mathbf{P} \cdot \mathbf{n} = \text{Re}_i \nabla \cdot \mathbf{n}. \tag{4}$$

Here $f(\bar{r},\bar{z},\bar{t}) = 0$ describes the *a priori* unknown free-surface shape, with the unit normal vector $\mathbf{n} = \nabla f/|\nabla f|$ pointing into the liquid, and the tensor $(\mathbf{I} - \mathbf{nn})$ extracts the component of a vector parallel to the surface with the normal $\mathbf{n}$.

At the plane of symmetry $\bar{z} = 0$, the standard symmetry conditions of impermeability and zero tangential stress are applied,

$$\mathbf{u} \cdot \mathbf{n}_s = 0, \quad \mathbf{n}_s \cdot \mathbf{P} \cdot (\mathbf{I} - \mathbf{n}_s\mathbf{n}_s) = \mathbf{0}, \tag{5}$$

where $\mathbf{n}_s$ is the unit normal to the plane of symmetry. In the conventional model we are studying here, the free surface is assumed to always be smooth so that where it meets the plane of symmetry we have $\mathbf{n} \cdot \mathbf{n}_s = 0$.

On the axis of symmetry, $\bar{r} = 0$, the standard normal and tangential velocity condition state that the velocity has only the component parallel to the $\bar{z}$-axis, and the radial derivative of this component is zero (the velocity field is smooth at

the axis),

$$\mathbf{u} \cdot \mathbf{n}_a = 0, \quad \frac{\partial}{\partial \bar{r}}[\mathbf{u} \cdot (\mathbf{I} - \mathbf{n}_a \mathbf{n}_a)] = \mathbf{0}, \quad \bar{r} = 0, \qquad (6)$$

where $\mathbf{n}_a$ is the unit normal to the axis of symmetry in the $(\bar{r}, \bar{z})$ plane.

For the case of coalescing free spheres, the free surface is assumed to be smooth at the apex, $\bar{r} = 0, \bar{z} = h(\bar{t})$, so that $\mathbf{n} \cdot \mathbf{n}_a = 0$ there, while the case of coalescing pinned hemispheres requires more conditions to account for the presence of the syringe. Specifically, at the point in the $(\bar{r}, \bar{z})$ plane where the (initially hemispherical) free surface meets the syringe tip, we have a pinned contact line,

$$f(1, 1, \bar{t}) = 0 \quad (\bar{t} \geqslant 0). \qquad (7)$$

It is assumed that in the far field, the liquid inside the syringe is at rest, so that

$$\mathbf{u} \to \mathbf{0} \quad \text{as} \quad \bar{r}^2 + \bar{z}^2 \to \infty, \qquad (8)$$

while on the cylinder's surface, no-slip is applied,

$$\mathbf{u} = \mathbf{0} \quad \text{at} \quad \bar{r} = 1, \quad \bar{z} \geqslant 1. \qquad (9)$$

Computations are started from a finite initial bridge radius $\bar{r}_{\min}$, and the details of the initial conditions can be very important when considering the initial stages of motion [8]. However, when considering the global motion of the drops, so long as $\bar{r}_{\min}$ is sufficiently small, say $\bar{r}_{\min} < 10^{-2}$, the subtleties surrounding the implementation of the initial conditions are unimportant. Our computations are started from $\bar{r}_{\min} = 10^{-4}$, and as an initial condition for the free surface we take a shape that provides a smooth free surface at $\bar{r} = \bar{r}_{\min}$ (which a truncated sphere would not), while far away from the origin (i.e., from the point of the initial contact) it is initially the undisturbed hemispherical or spherical drop. A shape that satisfies these criteria can be taken from [13], i.e., the analytic two-dimensional solution to the problem for Stokes flow. In parametric form, the initial free-surface shape is taken to be

$$\bar{r}(\theta) = \sqrt{2}(1 + m)H \cos\theta,$$

$$\bar{z}(\theta) = \sqrt{2}(1 - m)H \sin\theta, \qquad (10)$$

$$H = \{(1 - m^2)(1 + m^2)^{-1/2}[1 + 2m\cos(2\theta) + m^2]^{-1}\}$$

for $0 < \theta < \theta_u$, where m is chosen such that $\bar{r}(0) = \bar{r}_{\min}$ is the initial bridge radius, which we choose, and θ_u is chosen such that $\bar{r}(\theta_u) = \bar{z}(\theta_u) = 1$ for hemispherical drops and $\bar{r}(\theta_u) = 0$ for spherical ones. Notably, for $\bar{r}_{\min} \to 0$ we have $m \to 1$ and $\bar{r}^2 + (\bar{z} - 1)^2 = 1$, i.e., the drop's profile is a semicircle of unit radius that touches the plane of symmetry at the origin, as required.

Finally, we assume that the fluid starts from rest:

$$\mathbf{u} = \mathbf{0} \quad \text{at} \quad \bar{t} = 0. \qquad (11)$$

III. COMPUTATIONAL APPROACH

The coalescence phenomenon requires the solution of a free-boundary problem with effects of viscosity, inertia, and capillarity all present, so that a computational approach is

unavoidable. To do so, we use a finite-element framework that was originally developed for dynamic wetting flows and has been thoroughly tested in [14,15] as well as being applied to flows undergoing high free-surface deformation in [16], namely microdrop impact onto and spreading over a solid surface. Notably, the method implemented in our computational platform has been specifically designed for multiscale flows, so that the very small length scales associated with the early stages of coalescence can be captured alongside the global dynamics of the two drops' behavior. In other words, all of the spatiotemporal scales present in electrical measurements [6], as well as the scales associated with later stages of the drop's evolution, which are of interest here, can be simultaneously resolved. A user-friendly step-by-step guide to the implementation of the method can be found in [14,15], while benchmark coalescence simulations are provided in [8].

IV. RESULTS

A. Identifying an inertial regime

In Fig. 3, our computed solutions show that for $\mathrm{Re}_i \geqslant 10^2$ (curves 2, 3a, and 3b) the evolution of the bridge between the drops becomes insensitive to further increase in the Reynolds number until the dimensionless radius of the bridge, $\bar{r}_b \approx 0.75$. Deviations for very small bridge radii, $\bar{r}_b < \mathrm{Re}_i^{-1} \leqslant 10^{-2}$, caused by viscous forces being non-negligible and usually observed on a log-log plot, will not be important in the regime upon which we are focusing. In this regime, hemispheres pinned to the rim of the syringe needles and free spheres (curves 3a and 3b, respectively) give the same results [17]. This suggests that we are truly in an "inertial regime" in which (a) the effects of viscosity are negligible and (b) the process can be considered as "local," i.e., independent of the far-field geometry. It is in this regime that scaling law (1) is expected to approximate the exact solution and has often been used to interpret experimental data [4–6].
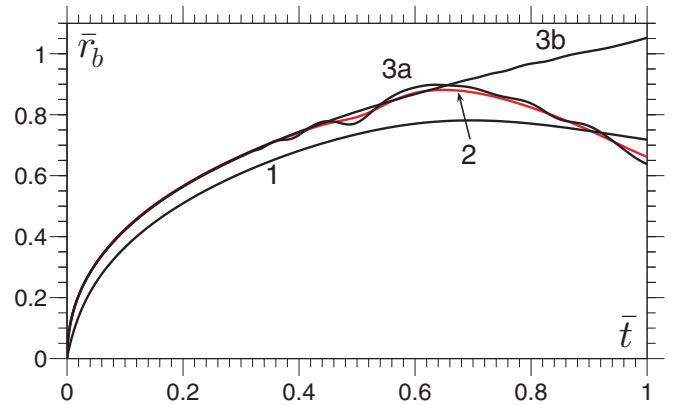

FIG. 3. (Color online) Identification of the "inertial regime" showing that above a critical Reynolds number, there is a period in which the bridge's evolution is independent of the value of Re_i or of the flow configuration. Pinned hemispheres are used in computations for 1: $\mathrm{Re}_i = 10$, 2: $\mathrm{Re}_i = 10^2$ (in red), 3a: $\mathrm{Re}_i = 10^3$, while curve 3b is for a free sphere with $\mathrm{Re}_i = 10^3$.
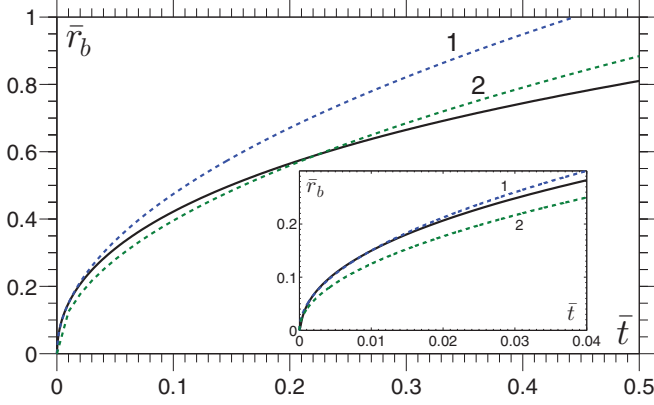
FIG. 4. (Color online) Comparison of the computed solution (solid line) to Eq. (1) with $C_i = 1.5$ (curve 1 in blue) and $C_i = 1.25$ (curve 2 in green).

B. Standard scalings

In Fig. 4, we can see that scaling law (1) with $C_i = 1.5$ (curve 1) provides a good approximation of the computed solution (solid line) for $\bar{r}_b < 0.15$. However, the scaling law quickly begins to overshoot the numerical solution. Worryingly, most comparisons between this scaling law and experimental data have been in the range accessible to optical observation, $\bar{r}_b > 0.1$ (which for a millimeter-sized drop is $r_b = 100\,\mu m$), whereas our computations show that the scaling law greatly overshoots the computed solution. In other words, it has been used *outside* the region where it gives a reasonable approximation of the solution of the mathematical problem it is supposed to mimic.

If instead we look to "fit" the whole of the computed curve in the region $0.1 < \bar{r}_b < 0.75$ as best as we can, ignoring large errors for $\bar{r}_b < 0.1$, then the result is that the prefactor must have a much smaller value of $C_i = 1.25$ (curve 2 in Fig. 4), the value that is closer to those obtained in previous experimental works [4,5] that fitted (1).

The upshot of the discrepancy between the scaling law and the computed solution in the experimental range is that reported values of C_i have been too small. Although a value of $C_i = 1.25$, consistent with those obtained from experimental analysis [4,5], provides a "best fit" (curve 2 in Fig. 4) for $0.1 < \bar{r}_b < 0.75$ to the exact solution (solid line), and hence also to the experimental data (Fig. 6), as can be seen from Fig. 4, this solution completely fails to capture the correct behavior as $\bar{r}_b \to 0$, where the scaling law should asymptotically approach the exact solution (solid curve).

The failure of the "best fit" approach is confirmed in Fig. 5, where the relative percentage error $E_b(\bar{t}) = 100|\bar{r}_{sc} - \bar{r}_{co}|/\bar{r}_{co}$ of the scaling laws $\bar{r}_b = \bar{r}_{sc}(\bar{t})$ from the computed solution $\bar{r}_b = \bar{r}_{co}(\bar{t})$ is plotted as a function of time. One can see that the scaling law (1) with $C_i = 1.5$ approximates the computed solution well, with $E_b < 3\%$ for $\bar{t} < 2 \times 10^{-2}$, while during the same time period $E_b > 15\%$ for curve 2, which is the "best fit" attempt $C_i = 1.25$ in (1). The error also confirms that while (1) with $C_i = 1.5$ captures the correct behavior in the inertial regime for small times, this solution rapidly departs from the computed solution, with $E_b > 12\%$ for $\bar{t} > 0.1$. If, as a crude estimate, we require a scaling law to satisfy
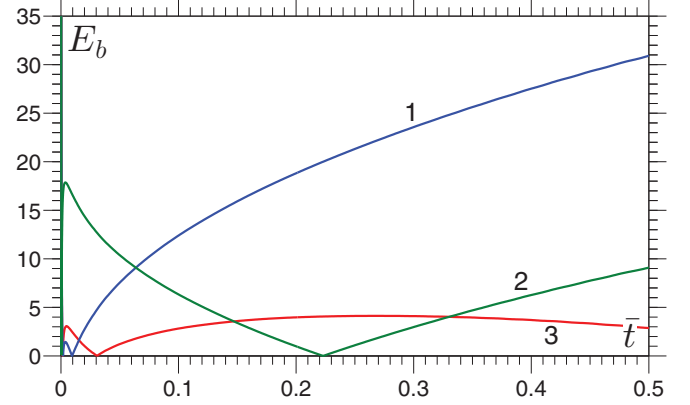

FIG. 5. (Color online) The relative percentage error E_b of the scaling laws from the computed solution. Curve 1 (in blue) is for (1) with $C_i = 1.5$, curve 2 (in green) is (1) taking $C_i = 1.25$, and curve 3 (in red) is (15) with $C_i = 1.5$.

$E_b < 5\%$, then we see that curve 1 meets this criterion for $\bar{t} < 0.03$ while curve 2 fails in the initial stages and is only valid for $0.12 < \bar{t} < 0.36$. Thus, neither of the current scaling laws provides satisfactory approximations to the computed solutions that could be used for a quick comparison between experimental and theoretical predictions.

Here, we will look to rectify the aforementioned inconsistencies by extending the scaling law (1), using the approach initiated in [3], to account for the azimuthal curvature, which reduces the capillary pressure and hence acts to slow down the evolution of the bridge, as well as the longitudinal curvature that drives the process. Although, as we shall see, the latter dominates as $\bar{r}_b \to 0$, it is anticipated that, by including the azimuthal curvature in the scaling law, we will be able to increase the region of applicability of our scaling to within the optical range. This should give a more accurate representation of the bridge evolution in the inertial regime, and it can be used to predict the speed of coalescence without having to resort to computations.
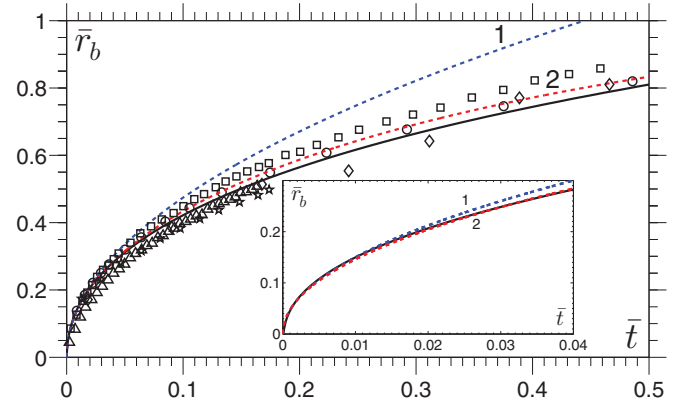

FIG. 6. (Color online) Comparison of the computed solution (solid black curve) of free spheres coalescing with $Re_i = 10^3$ to Eq. (1) with $C_i = 1.5$ (curve 1 in blue) and the new scaling (15) also with $C_i = 1.5$ (curve 2 in red). Data have been obtained from the lowest viscosity drops considered in the following publications: circles, Fig. 3 F in [1]; squares, Fig. 6 in [3]; triangles, Fig. 3 a in [5]; diamonds, Fig. 6 in [2]; and stars, best-fit to Fig. 4 in [4].

C. An improved scaling

Including the curvature at the bridge front in the azimuthal direction, i.e., $\bar{\kappa}_2 = -1/\bar{r}_b$, which acts to resist the bridge's outward motion, into our expression for the full curvature $\bar{\kappa}$ is simple; however, as a consequence of this extension, we must specify how the longitudinal curvature $\bar{\kappa}_1$ scales as the bridge propagates, since we are no longer able to "absorb" this scale into the constant of proportionality. Thus, we now have

$$\bar{\kappa} = \bar{\kappa}_1 + \bar{\kappa}_2 = \frac{A}{\bar{r}_b^2} - \frac{1}{\bar{r}_b}, \quad (12)$$

where the constant A must be specified to account for the longitudinal curvature behavior as the bridge expands. Previously, i.e., in (1), the second term on the right-hand side was neglected and this constant was simply absorbed into C_i. If the undisturbed free-surface height at $\bar{r}_b$ is taken as the radius of curvature at that point, then, for small $\bar{r}_b$, we have $A = 2$. However, in [3], it is argued that $A \approx 1$ gives a better agreement with experiments as with this value the radius of curvature is the distance between the two undisturbed free surfaces rather than the distance from the plane of symmetry to one of them, and hence it accounts for the "bulb which develops at the end of the advancing interface." This assertion is confirmed by our computations shown in the Appendix, and so, henceforth, we assume $A = 1$ and, if needs be, we can later consider whether more accurate representations of A are required. In [3], the resulting equations, which considered drops of different sizes, were solved using a numerical method and seen to give good agreement with the experimental data.

In the case of the coalescence of two identical liquid drops, with curvature given by (12), it will be shown that an analytic solution can be obtained that, now that A has been specified, still contains only one free constant. As proposed in [9], balancing (dimensionless) inertial forces with the (driving) surface tension force gives

$$\left(\frac{d\bar{r}_b}{d\bar{t}}\right)^2 = \frac{C_i^4}{4}\left(\frac{1}{\bar{r}_b^2} - \frac{1}{\bar{r}_b}\right), \quad (13)$$

where the coefficient of proportionality has been chosen so that if the azimuthal curvature is ignored, we recover $\bar{r}_b = C_i \bar{t}^{1/2}$. Integrating (13), assuming that $\bar{r}_b = 0$ at $\bar{t} = 0$ [18], and rearranging, we obtain a cubic polynomial in $\bar{r}_b$ with $\bar{t}$ as a parameter:

$$\bar{r}_b^3 + 3\bar{r}_b^2 + \frac{3C_i^2\bar{t}}{4}\left(\frac{3C_i^2\bar{t}}{4} - 4\right) = 0. \quad (14)$$

We can see immediately that if only the leading-order terms in $\bar{r}_b$ and $\bar{t}$ are kept, we have $3\bar{r}_b^2 - 3C_i^2\bar{t} = 0$ so that the usual scaling (1) is recovered. The solution that we require is given by

$$\bar{r}_b = \frac{s}{4} + \frac{4}{s} - 1, \quad s = [-64 - 18d^2 + 96d + 2(2880d^2$$
$$- 3072d + 81d^4 - 864d^3)^{1/2}]^{1/3}, \quad d = C_i^2\bar{t}, \quad (15)$$

where we take the root with the positive imaginary part for s [19], which results in $\bar{r}_b$ being real.

D. Comparison of the improved scaling law to simulations and experiments

The explicit form of (15) allows for a quick comparison with a computed solution or experiments, with no additional fitting parameters, in order to determine whether this is a significant improvement on (1). In the inset of Fig. 6, it can be clearly seen that for the same value of $C_i = 1.5$, the new scaling law (curve 2) gives results indistinguishable from those given by (1) (curve 1) for $\bar{r}_b < 0.15$ but for $0.15 < \bar{r}_b < 0.8$ (shown in the main plot), i.e., for the range usually used in experimental works to fit a scaling law to the data, the new expression agrees far better with the simulation of the full system (solid line computed for free spheres) than the expression (1). This is confirmed in Fig. 5, where it can be seen that the new scaling law is within 5% of the computed solution at least up to $\bar{t} = 0.5$. Although curve 2 is not indistinguishable from the numerical result for $\bar{r}_b > 0.4$ in Fig. 6, as one may expect from the simplifications made, as an approximating formula it is a significant improvement on the previous result and is close to the numerical solution for a remarkably large proportion of the coalescence process.

In Fig. 6, it can be clearly seen that the new "universal curve" (curve 2) is able to capture experimental data for the inertial regime collected from the literature for completely different geometric configurations (hanging pendent drops, pinned hemispheres, and spheres supported by a hydrophobic solid) and thus provides the sought-after extension to (1) required to approximate the coalescence dynamics in this regime while retaining a simple analytic expression.

In Fig. 1, we can see that the initial dynamics of coalescence in the inertial regime is genuinely "local," as the two different geometries used for experiments (pendent drops) and simulations (free spheres) agree for the initial stages of motion, i.e., the deformed free surface in both the experiment and the simulation agree perfectly even though their entire shapes, by construction, do not. It is only around $\bar{t} = 0.3$ that the free surface shapes in the bridge region start to feel their entire geometry, so that the inertial regime is essentially over as the bridge's propagation is no longer "local." Despite this, it is seen from Fig. 6 that the estimates for the bridge radius stay close to the exact solution and the experimental data for a considerably longer time, remaining relatively accurate until at least $\bar{t} = 0.5$, at which point $\bar{r}_b \approx 0.8$.

A shortcoming of the obtained expression is that it does not include the influence of gravity on the drops' evolution, which manifests itself most strongly by altering the initial shape of drops. This effect will be significant for drops larger than the capillary length, which for water is of the order of millimeters. However, for smaller low-viscosity drops, particularly those from around $R = 10\ \mu$m to $R = 1$ mm, where inertial effects still dominate viscous ones, the expression in (15) will provide an excellent approximation to their evolution.

APPENDIX: COMPUTATION OF THE LONGITUDINAL CURVATURE

Figure 7 shows the free-surface shape obtained from the computed solution for free spheres coalescing at $Re_i = 10^3$ in the range $0.1 \leqslant \bar{r}_b \leqslant 0.7$. Marked with crosses are the point on the free surface at which the longitudinal curvature $\bar{\kappa}_1$ changes
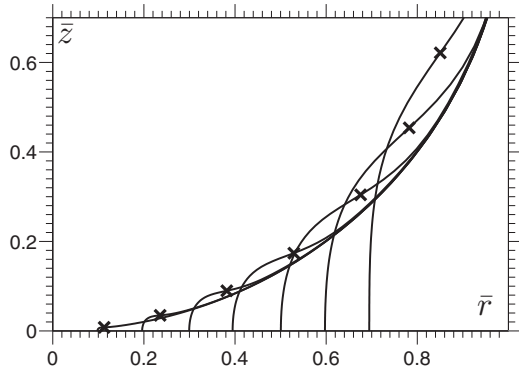
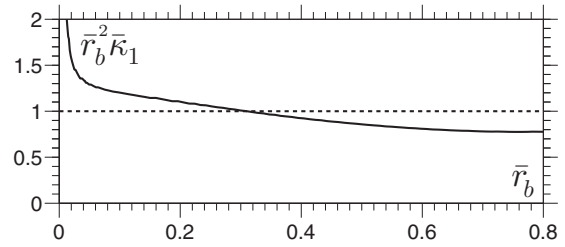FIG. 7. Snapshots of the coalescence process showing crosses at the inflection point on the free surface.

FIG. 8. Evolution of the computed effective longitudinal curvature of the bridge connecting the coalescing drops $\bar{\kappa}_1$ multiplied by the square of the bridge radius $\bar{r}_b^2$. It can be seen that $\bar{\kappa}_1 \bar{r}_b^2 \approx 1$ as assumed.

sign, i.e., the crosses mark an inflection point in the free-surface profile. The height of this inflection point, $\bar{z} = \bar{z}_{\text{inf}}$, can be used to define the *effective* longitudinal curvature of the bridge connecting the coalescing drops as $\bar{\kappa}_1 = 1/\bar{z}_{\text{inf}}$. This allows us to test the assumption that $\bar{\kappa}_1 \approx 1/\bar{r}_b^2$, or alternatively that $\bar{\kappa}_1 \bar{r}_b^2 \approx 1$.

In Fig. 8, it can be seen that in the range $0.1 \leqslant \bar{r}_b \leqslant 0.7$ we have $\kappa_1 \bar{r}_b^2$ approximately constant, so that the assumed scaling behavior sufficiently accurately reflects the exact solution: over the period considered, it is in the range $\kappa_1 \bar{r}_b^2 \in (0.8, 1.2)$, so that its average value will be close to 1. Slight improvements could potentially be achieved by using a linear approximation for the curvature, but given the good agreement between the new scaling and the fully computed results, this does not seem necessary.

[1] J. D. Paulsen, J. C. Burton, S. R. Nagel, S. Appathurai, M. T. Harris, and O. Basaran, Proc. Natl. Acad. Sci. U.S.A. **109**, 6857 (2012).

[2] A. Menchaca-Rocha, A. Martínez-Dávalos, R. Núńez, S. Popinet, and S. Zaleski, Phys. Rev. E **63**, 046309 (2001).

[3] S. T. Thoroddsen, K. Takehara, and T. G. Etoh, J. Fluid Mech. **527**, 85 (2005).

[4] M. Wu, T. Cubaud, and C. Ho, Phys. Fluids **16**, L51 (2004).

[5] D. G. A. L. Aarts, H. N. W. Lekkerkerker, H. Guo, G. H. Wegdam, and D. Bonn, Phys. Rev. Lett. **95**, 164503 (2005).

[6] J. D. Paulsen, J. C. Burton, and S. R. Nagel, Phys. Rev. Lett. **106**, 114501 (2011).

[7] K. Fezzaa and Y. Wang, Phys. Rev. Lett. **100**, 104501 (2008).

[8] J. E. Sprittles and Y. D. Shikhmurzaev, Phys. Fluids **24**, 122105 (2012).

[9] J. Eggers, J. R. Lister, and H. A. Stone, J. Fluid Mech. **401**, 293 (1999).

[10] A. B. Thompson and J. Billingham, IMA J. Appl. Math. **77**, 678 (2012).

[11] L. Duchemin, J. Eggers, and C. Josserand, J. Fluid Mech. **487**, 167 (2003).

[12] L. Baroudi, M. Kawaji, and T. Lee, Comput. Math. Appl. **67**, 282 (2014).

[13] R. W. Hopper, J. Am. Ceram. Soc. **67**, C-262 (1984).

[14] J. E. Sprittles and Y. D. Shikhmurzaev, Int. J. Numer. Methods Fluids **68**, 1257 (2012).

[15] J. E. Sprittles and Y. D. Shikhmurzaev, J. Comput. Phys. **233**, 34 (2013).

[16] J. E. Sprittles and Y. D. Shikhmurzaev, Phys. Fluids **24**, 082001 (2012).

[17] It is the capillary waves, initiated at the onset of coalescence, traveling along the free surface and interacting with the far-field boundary, that eventually "kill" the local nature of the solution in this regime.

[18] A finite radius of contact could easily be added, but experiments demonstrate that this radius is very small, so that its inclusion would have almost no effect on the resulting evolution in the regime of interest.

[19] This is the default root for most software, e.g., MATLAB.